Nanoscale

RSC Publishing

COMMUNICATION

View Article Online
View Journal | View Issue

Cite this: *Nanoscale*, 2013, **5**, 4657

Co_3O_4 nanoparticle-modified MnO_2 nanotube bifunctional oxygen cathode catalysts for rechargeable zinc–air batteries†

Received 17th January 2013
Accepted 31st March 2013

DOI: 10.1039/c3nr00300k

www.rsc.org/nanoscale

Guojun Du,[ab] Xiaogang Liu,*[ab] Yun Zong,[a] T. S. Andy Hor,[ab] Aishui Yu[c] and Zhaolin Liu*[a]

We report the preparation of MnO_2 nanotubes functionalized with Co_3O_4 nanoparticles and their use as bifunctional air cathode catalysts for oxygen reduction reaction and oxygen evolution reaction in rechargeable zinc–air batteries. These hybrid MnO_2/Co_3O_4 nanomaterials exhibit enhanced catalytic reactivity toward oxygen evolution reaction under alkaline conditions compared with that in the presence of MnO_2 nanotubes or Co_3O_4 nanoparticles alone.

1 Introduction

Zinc–air batteries (ZABs) have drawn increasing attention in recent years due to their environmentally benign manufacturing, low operation risks, and high specific energy in excess of 400 W h kg^{-1} and 650 W h L^{-1} in coin-cell configuration.[1–3] ZABs are mainly composed of three parts: zinc metal as the anode, an air electrode as the cathode, and a membrane that separates the anode and the cathode. In ZABs, oxygen in gas phases such as air is applied due to the limited solubility of oxygen molecules in solvents at atmospheric pressure. The diffusion of oxygen from the atmosphere into the air electrode is triggered by different oxygen pressures between the outside and inside of the cell. Subsequently, the catalyst facilitates the reduction of oxygen to hydroxyl ions in an alkaline electrolyte with electrons generated from the oxidation of zinc metals in the anodic reaction. Despite their enormous promise for commercialization, there are several major technical challenges associated with ZABs. Critical challenges limiting the practical use of this technology include sluggish oxygen reduction reaction (ORR), low oxygen evolution reaction (OER) kinetics, and a large overpotential. Therefore, a key solution is to develop novel bifunctional electrocatalysts that are effective for both ORR and OER processes.

The air electrode is known to be a strongly irreversible system with a high activation overvoltage in aqueous solutions. Although noble metal catalysts such as platinum have high reactivity for ORR and OER, the cost of manufacturing noble metal based air cathodes is high. Benefiting from relatively facile oxygen reduction in alkaline solutions, ZABs utilizing alkaline solutions do not need a pure noble metal catalyst.[4,5] Non-precious metal catalysts including organometallic compounds,[6] transition metal oxides (such as perovskite, pyrochlore and spinel, individual oxides, and their mixtures)[7–17] and carbon based materials (like graphene and nitrogen-doped carbon nanotubes)[18,19] could be used to improve the performance of ZABs. Among these non-precious metal catalysts, MnO_2 is presently being considered as the most promising electrocatalyst toward the ORR in alkaline solutions because of its relatively high catalytic activity, good stability against corrosion, and low cost.[20] Besides, transition metal oxides, such as spinel Co_3O_4 and $M_xCo_{3-x}O_4$ (M = Cu, Ni), could also be used as electrocatalysts for OER.[21–25] Recently, spinel-structured Co–Mn–O nanocrystals, which possess high surface area, numerous defects and abundant vacancies, show remarkable reactivity toward the ORR/OER couple.[26] We hence anticipate that the combination of MnO_2 and Co_3O_4 nanocrystals could lead to the production of bifunctional electrocatalysts[27] with substantially improved electrocatalytic activity for both ORR and OER. In principle, this design concept can be applied to both one-dimensional (1-D) nanostructures such as nanotubes and zero-dimensional (0-D) nanostructures such as nanospheres. For the air cathode, one-dimensional (1-D) nanotubes rather than zero-dimensional (0-D) particles as electrode catalysts offer several advantages:[28,29] (i) better charge transport ability, (ii) low mass loading, (iii) better mass transport of the solvated ions, and (iv) better mechanical toughness. In this work, we demonstrate the

[a]*Institute of Materials Research and Engineering (IMRE), Agency of Science, Technology, and Research (A*STAR), 3 Research Link, Singapore 117602, Singapore. E-mail: zl-liu@imre.a-star.edu.sg; Fax: +65 68720785; Tel: +65 68727532*

[b]*Department of Chemistry, National University of Singapore, 3 Science Drive 3, Singapore 117543, Singapore. E-mail: chmlx@nus.edu.sg*

[c]*Department of Chemistry, Shanghai Key Laboratory of Molecular Catalysis and Innovative Materials, Institute of New Energy, Fudan University, Shanghai 200438, China*

† Electronic supplementary information (ESI) available: Zinc–air cell device, XPS survey scan and power density of the cell. See DOI: 10.1039/c3nr00300k

coating of MnO_2 nanotubes with Co_3O_4 nanocrystals and investigate their use in rechargeable ZABs.

2 Experimental

2.1 Synthesis of MnO_2/Co_3O_4 hybrid nanomaterials

All the reagents were of analytical purity and were used without further purification. First, MnO_2 nanotubes were prepared by a facile hydrothermal method.[30] In a typical experiment, 2.5 mmol $KMnO_4$ and 10 mmol concentrated HCl were added to 25 mL deionized water to form the precursor solution, and then the solution was transferred into a 50 mL Teflon-lined stainless steel autoclave. The autoclave was sealed and hydrothermally treated at 140 °C for 12 h. After the autoclave was cooled down to room temperature naturally, the samples were collected and washed several times with ethanol and deionized water. The as-prepared products were dried in air at 70 °C overnight for further modification. Then Co_3O_4 nanoparticles were modified on the MnO_2 nanotubes by a hydrothermal method combined with post-heat treatment. In a typical synthesis of MnO_2/Co_3O_4 hybrid nanomaterials, 0.25 g $Co(CH_3COO)_2 \cdot 4H_2O$ was dissolved in 15 mL of 1.3 mol L^{-1} ammonia solution. Afterwards, 0.25 g as-prepared MnO_2 nanotubes were dispersed in the above solution by ultrasonication for 10 min. This mixture was then transferred into a 20 mL autoclave. Then the autoclave was sealed and maintained at 150 °C for 5 h. The resulting products were separated by centrifugation, washed with deionized water, dried at 60 °C for 5 h, and then calcined in air at 300 °C for 1 h. During the process of Co_3O_4 modification, the Co^{2+} ions were first deposited onto the surface of the MnO_2 nanotubes in the form of $Co(OH)_2$ under alkaline and hydrothermal conditions.[31] After calcination at 300 °C in air, $Co(OH)_2$ was subsequently decomposed into Co_3O_4 nanoparticles.

2.2 Characterization

X-ray diffraction (XRD) measurements were taken using an X-ray diffractometer (Bruker D8 GADDS) with Cu Kα (λ = 0.15406 nm). Scanning electron microscopy (SEM) images were obtained using a JEOL JSM-6700F microscope. The amount of Mn and Co element was determined using an Oxford INCA Energy Dispersive X-ray (EDX) spectrometer. Transmission Electron Microscopy (TEM) characterization was performed using a Philips CM300-FEG instrument with operating voltage at 300 kV. X-ray photoelectron spectroscopy (XPS) data were recorded with a Theta Probe electron spectrometer from Thermo Scientific using Al Kα ($h\nu$ = 1484.6 eV) radiation. The binding energies were corrected by the C 1s line at 285.0 eV from adventitious carbon.

2.3 Electrode preparation and electrochemical measurements

A rotating disc electrode (RDE) half-cell setup was used to investigate the ORR and OER catalytic activity of the samples. The working electrode was fabricated by casting Nafion-impregnated catalyst ink onto a glassy carbon disk electrode (5 mm in diameter). 10 mg of the catalyst was ultrasonically dispersed into 1 mL 0.5 wt% Nafion solution to form a catalyst ink. 10 μL of the catalyst ink was deposited on the disk and dried at room temperature. The working electrode was allowed to achieve a catalyst loading of 0.1 mg cm^{-2}. Electrochemical activity of the samples was studied using linear sweep voltammetry. The working electrode was immersed in a glass cell containing 0.1 M KOH aqueous electrolyte. A platinum foil and an Ag/AgCl electrode were used as the counter and reference electrodes, respectively. Catalyst activity toward the ORR was evaluated in oxygen-saturated electrolyte solution from 1.1 to 0.1 V *vs.* RHE. The catalytic performance for OER was measured in the electrolyte solution from 1.1 to 1.9 V *vs.* RHE. The potential of the reference electrode was normalized with respect to the potential of the reversible hydrogen electrode (RHE). The rotation rate is 2000 rpm and the scan rate is 5 mV s^{-1}. A commercial Pt/C catalyst (30 wt% platinum on carbon) was tested using the same procedure.

A home-made zinc–air cell device was designed for the battery test. As shown in Fig. S1,† the air electrode was prepared by spraying the catalyst onto a gas diffusion layer (SGL Carbon paper, Germany, 2 cm × 2 cm) to achieve a loading of 2 mg cm^{-2}. The electrolyte used in the zinc–air battery was 6 M KOH, and a polished zinc plate was used as the anode. Battery testing and cycling experiments were performed at 25 °C using the recurrent galvanic pulse method, where one cycle consisted of a discharging step (15 mA cm^{-2} for 7 min) followed by a charging step of the same current and duration time.

3 Results and discussion

The morphologies of the products were firstly examined using a field-emission gun scanning electron microscope (FESEM) and a transmission electron microscope (TEM). Fig. 1a shows the typical SEM image of the as-synthesized MnO_2 nanotubes, which indicates that the length of the nanotubes is in the range of 1–2 μm. The TEM image indicates that the diameter and wall thickness of a single MnO_2 tube are about 50 and 14 nm, respectively (Fig. 1c). Fig. 1b and d are the corresponding SEM and TEM images of the hybrid Co_3O_4-modified MnO_2 nanotubes, showing homogeneous coating of the Co_3O_4 nanoparticles on the surface of the MnO_2 nanotubes. The average size of the Co_3O_4 nanoparticles is about 10 nm. Fig. 1e shows a high resolution transmission electron microscopy (HRTEM) image of the interface between a single MnO_2 nanotube and Co_3O_4 nanocrystals. The observed lattice spacing of 0.69 nm corresponds to the (110) plane of tetragonal α-MnO_2 (Joint Committee on Powder Diffraction Standards file no. 41-0141). The HRTEM image of the nanoparticles reveals a lattice fringe of the (311) plane with a *d*-spacing of 0.24 nm, typical of cubic Co_3O_4 (Joint Committee on Powder Diffraction Standards file no. 76-1802).

Subsequently, the resulting Co_3O_4-modified MnO_2 nanotubes were characterized by energy-dispersive X-ray spectroscopy (EDS). Compositional analysis of the Co_3O_4-modified MnO_2 nanotube reveals that the MnO_2 and Co_3O_4 contents are 72 wt% and 28 wt%, respectively (Fig. 2a). The X-ray diffraction (XRD) patterns of the MnO_2 nanotubes and their Co_3O_4-modified

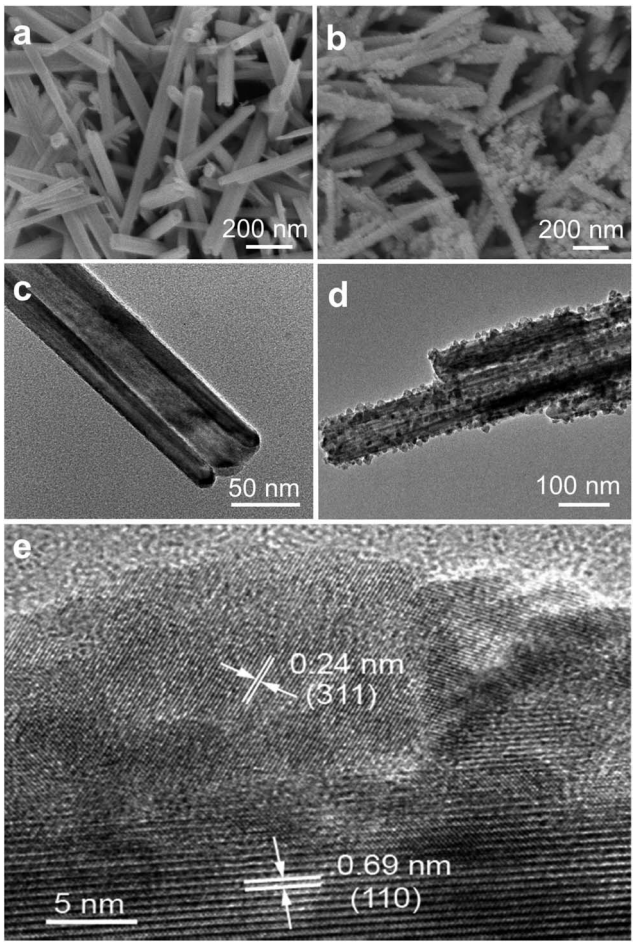

Fig. 1 SEM images of the MnO_2 nanotubes (a) and MnO_2/Co_3O_4 hybrid nanomaterials (b); TEM images of an individual MnO_2 nanotube (c) and MnO_2/Co_3O_4 hybrid materials (d); HRTEM image of the interface between a single MnO_2 nanotube and Co_3O_4 nanocrystals (e).

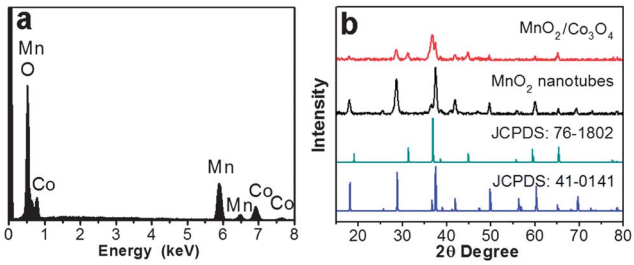

Fig. 2 EDS spectrum of the MnO_2/Co_3O_4 hybrid nanomaterials (a) and XRD patterns of the MnO_2 nanotubes and MnO_2/Co_3O_4 hybrid nanomaterials (b).

counterparts are shown in Fig. 2b. All major diffraction peaks match well with the standard peaks of tetragonal α-MnO_2 for the nanotube sample. For MnO_2/Co_3O_4 hybrid nanomaterials, the diffraction peaks at 31.3°, 36.9° and 44.9° can be indexed to (220), (311), and (400) planes of Co_3O_4, respectively.

We further utilized X-ray photoelectron spectroscopy (XPS) to probe the Mn, Co, O and C elements of the hybrid nanomaterials (*cf.* Fig. S2, ESI†). The carbon element is ascribed to traces of adventitious carbon. Fig. 3a shows the detailed scan of

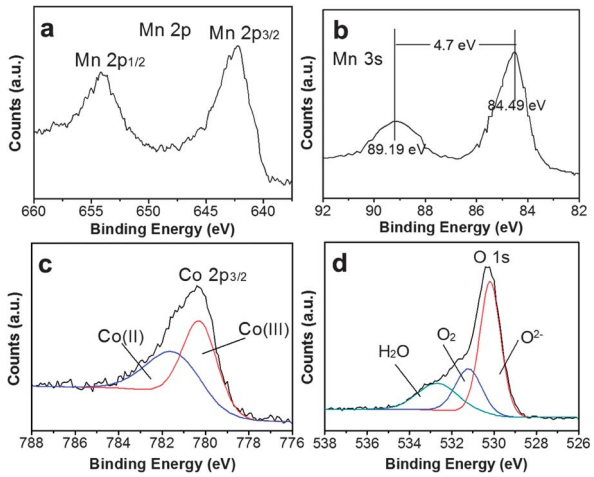

Fig. 3 High resolution XPS spectrum of Mn(2p) (a), Mn(3s) (b), Co(2p) (c) and O(1s) (d) regions.

Mn(2p). The Mn(2p) XPS spectrum exhibits two major peaks with binding energy values at 654.1 and 642.3 eV and a spin-energy separation of 11.8 eV, which are in good agreement with the reported data of $Mn(2p_{3/2})$ and $Mn(2p_{1/2})$ in MnO_2.[32] As reported previously,[33] the average oxidation state of Mn in manganese oxides can be determined by the separation of peak energies of the Mn(3s) peaks. The MnO_2/Co_3O_4 hybrid nanomaterials showed a separated energy of 4.7 eV for the Mn(3s) doublet (Fig. 3b), which suggests that the oxidation state of Mn in the composite is ~4.0. Fig. 3c displays the XPS spectrum of $Co(2p_{3/2})$. The $Co(2p_{3/2})$ component is centered at 780.3 eV with a full-width-at-half-maximum of 2.4 eV, which is in good agreement with the literature.[34,35] The two fitted peaks correspond to Co(III) and Co(II), respectively. The atomic ratio of Co(III)/Co(II) is close to 2, which is in agreement with the stoichiometric formula of the spinel cobalt oxide ($CoCo_2O_4$). The

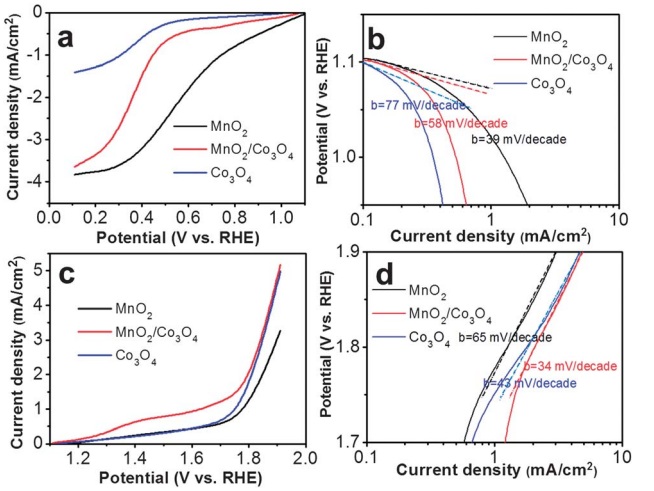

Fig. 4 ORR polarization curves of the MnO_2 nanotubes, Co_3O_4 nanoparticles and MnO_2/Co_3O_4 hybrid nanomaterials (a), Tafel plots of MnO_2 nanotubes, Co_3O_4 nanoparticles and MnO_2/Co_3O_4 hybrid nanomaterials (b), OER polarization curves of the MnO_2 nanotubes, Co_3O_4 nanoparticles and MnO_2/Co_3O_4 hybrid nanomaterials (c), and Tafel plots of OER currents in c (d).

fitted O(1s) spectrum is represented by three bands (Fig. 3d). The bands at 532.7 and 531.2 eV can be attributed to the oxygen and water molecules absorbed on the composite surface. The peak at 530.2 eV corresponds to the oxygen species comprising the MnO_2/Co_3O_4 hybrid nanomaterials.[35]

In a further set of experiments, we tested the catalytic activity of the as-prepared materials for ORR and OER activities by linear sweep voltammetry with a rotating disk electrode. As shown in Fig. 4a, the onset potential for Co_3O_4-modified MnO_2 nanotubes was detected at 1.05 V, whereas it was 0.90 V and 1.10 V for Co_3O_4 nanoparticles and MnO_2 nanotubes, respectively. At 0.2 V, Co_3O_4 nanoparticles and Co_3O_4-modified MnO_2 nanotubes afforded an ORR current density of ~1.3 mA cm^{-2} and 3.4 mA cm^{-2}, respectively, approaching that of the MnO_2 nanotubes (~3.7 mA cm^{-2}). The Tafel slope at low overpotentials of MnO_2 nanotubes, Co_3O_4-modified MnO_2 nanotubes and Co_3O_4 nanoparticles is 39, 58 and 77 mV per decade, respectively (Fig. 4b). On the basis of the onset potential, cathodic current and Tafel slope, MnO_2/Co_3O_4 hybrid nanomaterials are much more active than Co_3O_4 nanoparticles and slightly less active than the MnO_2 nanotubes for the ORR. The decrease of ORR activity could be attributed to the occupation of some active sites on MnO_2 nanotubes by Co_3O_4 nanoparticles. Apart from the ORR activity, excellent OER activity is particularly critical for bifunctional catalysts. As shown in Fig. 4c, the OER current density of MnO_2 nanotubes, MnO_2/Co_3O_4 hybrid nanomaterials and Co_3O_4 nanoparticles at 1.8 V was 1.3, 2.2 and 1.9 mA cm^{-2}, respectively. There is a small Tafel slope down to 34 and 43 mV per decade for Co_3O_4-modified MnO_2 nanotubes and Co_3O_4 nanoparticles compared with the MnO_2 nanotubes (Fig. 4d). The results indicate that the MnO_2/Co_3O_4 hybrid is more active than MnO_2 and Co_3O_4 for the OER activity. Furthermore, we compared our bifunctional catalysts with the commercial carbon-supported platinum nanoparticles (Pt/C). It is encouraging to note that the MnO_2/Co_3O_4 hybrid exhibits slightly less ORR and comparable OER activity compared to the commercial Pt/C catalyst (Fig. 5a and b). There is a slightly larger Tafel slope of 58 mV per decade for Co_3O_4-modified MnO_2 nanotubes compared with that of a Pt/C catalyst (33 mV per decade) for the ORR (Fig. 5c). Excellent OER activity of the MnO_2/Co_3O_4 hybrid nanomaterials was also found from the smaller Tafel slope of 34 mV per decade (Fig. 5d) than that measured with Pt/C (52 mV per decade). These results suggest that the high activity of the Co_3O_4-modified MnO_2 nanotubes for the ORR and OER may be due to the synergistic effect and the interface effect between the MnO_2 nanotubes and Co_3O_4 nanoparticles. Herein, the Co_3O_4 nanoparticles are responsible for high electrical conductivity and high OER activity while the MnO_2 nanotubes offer high performance for the ORR.

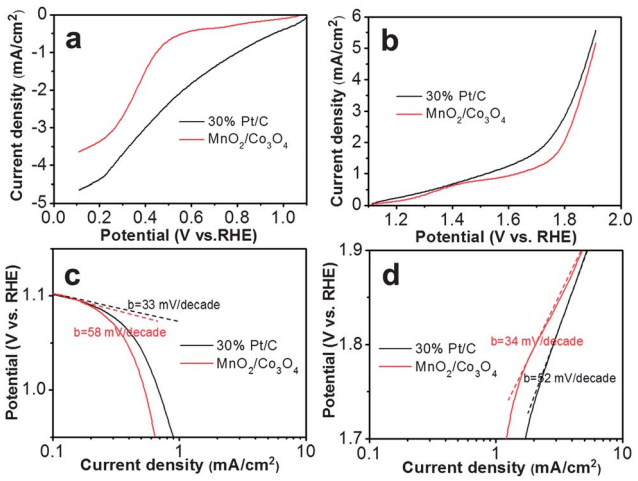

Fig. 5 ORR polarization curves (a) and OER polarization curves (b) of the 30 wt% Pt/C catalyst and MnO_2/Co_3O_4 hybrid materials. Tafel plots of ORR currents in a (c). Tafel plots of OER currents in b (d).

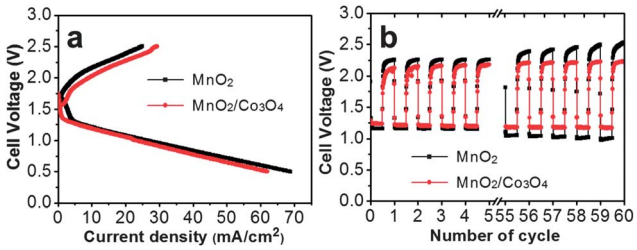

Fig. 6 Battery discharge and charge polarization curves of the MnO_2 nanotubes and MnO_2/Co_3O_4 hybrid nanomaterials (a) and performance of the battery charge–discharge cycling (b).

A galvanodynamic method was used to discharge and charge the testing single cell. The results of the MnO_2 nanotubes and MnO_2/Co_3O_4 catalysts are shown in Fig. 6a. The discharging curves illustrate an activation loss region followed by a pseudo-linear ohmic loss region. The MnO_2/Co_3O_4 hybrid nanomaterials show similar discharging activity with respect to MnO_2 nanotubes. Regarding the cell charging process, MnO_2/Co_3O_4 has a lower cell voltage at the same current density than MnO_2 nanotubes, indicating that the hybrid nanomaterials are more active than MnO_2 nanotubes as identified by the linear sweep test. The maximum power densities of the MnO_2 nanotubes and MnO_2/Co_3O_4 hybrid nanomaterials are 36 and 33 mW cm^{-2} at 25 °C (*cf.* Fig. S3, ESI†), which are superior to those reported (*e.g.* 30 mW cm^{-2} for the Ag/C nanoparticle catalyst[36] at 35 °C, 18 mW cm^{-2} for the MnO_2 catalyst[37] at 25 °C) and are comparable to the result (*e.g.* 35 mW cm^{-2} for the $PbMnO_x$ catalyst[37] at 25 °C).

The stability of the catalysts was examined through the charge–discharge cycling in 6 M KOH. A charge–discharge experiment was performed by discharging and charging (7 min in each state) the battery at 15 mA cm^{-2} using the recurrent galvanic pulse method. As shown in Fig. 6b, the first five cycles show almost the same discharge voltage and a lower charge plateau for the MnO_2/Co_3O_4 hybrid nanomaterials. The potential change in the charge and discharge process for the MnO_2 nanotubes after 60 cycles is 14% and 13%, respectively. With respect to MnO_2/Co_3O_4 hybrid nanomaterials, both the charge potential and discharge potential after 60 cycles varied by 5%. This result indicates that the combination of Co_3O_4 with MnO_2 nanotubes is effective for both reducing the charging potential and enhancing the cyclic stability simultaneously.

4 Conclusions

In summary, MnO_2/Co_3O_4 hybrid nanomaterials as a new air electrode material have been synthesized *via* a two-step hydrothermal method. These hybrid nanomaterials display good bifunctional ORR/OER activity and cyclic stability in the discharge and charge process. Further studies are ongoing to improve the ZAB performance by manipulating the hybrid structure.

This research was supported by the Advanced Energy Storage Research Programme (IMRE/12-2P0503), Institute of Materials Research and Engineering (IMRE/11-1C0218) of the Agency for Science, Technology and Research, and the National University of Singapore.

Notes and references

1 S. I. Smedley and X. G. Zhang, *J. Power Sources*, 2007, **165**, 897.
2 P. Sapkota and H. Kim, *J. Ind. Eng. Chem.*, 2009, **15**, 445.
3 Z. Chen, J. Choi, H. Wang, H. Li and Z. W. Chen, *J. Power Sources*, 2011, **196**, 3673.
4 L. Jörissen, *J. Power Sources*, 2006, **155**, 23.
5 J. S. Lee, S. T. Kim, R. Cao, N. S. Choi, M. Liu, K. T. Lee and J. Cho, *Adv. Energy Mater.*, 2011, **1**, 34.
6 S. Zhang, X. Z. Yuan, J. N. C. Hin, H. Wang, K. A. Friedrich and M. Schulz, *J. Power Sources*, 2009, **194**, 588.
7 V. Neburchilov, H. Wang, J. J. Martin and W. Qu, *J. Power Sources*, 2010, **195**, 1271.
8 M. Hamdani, R. N. Singh and P. Chartier, *Int. J. Electrochem. Sci.*, 2010, **5**, 556.
9 V. Nikolova, P. Iliev, K. Petrov, T. Vitanov, E. Zhecheva, R. Stoyanova, I. Valov and D. Stoychev, *J. Power Sources*, 2008, **185**, 727.
10 B. Wang, *J. Power Sources*, 2005, **152**, 1.
11 J. Suntivich, H. A. Gasteiger, N. Yabuuchi, H. Nakanishi, J. B. Goodenough and Y. Shao-Horn, *Nat. Chem.*, 2011, **3**, 546.
12 K. Miyazaki, K. Kawakita, T. Abe, T. Fukutsuka, K. Kojima and Z. Ogumi, *J. Mater. Chem.*, 2011, **21**, 1913.
13 M. Yuasa, M. Nishida, T. Kida, N. Yamazoe and K. Shinoe, *J. Electrochem. Soc.*, 2011, **158**, A605.
14 E. Rios, H. Reyes, J. Ortiz and J. L. Gautier, *Electrochim. Acta*, 2005, **50**, 2705.
15 M. D. Koninck, S. C. Poirier and B. Marsan, *J. Electrochem. Soc.*, 2006, **153**, A2103.
16 F. Y. Cheng, Y. Su, J. Liang, Z. L. Tao and J. Chen, *Chem. Mater.*, 2010, **22**, 898.
17 Y. Gorlin and T. F. Jaramillo, *J. Am. Chem. Soc.*, 2010, **132**, 13612.
18 L. Qu, Y. Liu, J. B. Baek and L. Dai, *ACS Nano*, 2010, **4**, 1321.
19 S. Zhu, Z. Chen, B. Li, D. Higgins, H. Wang, H. Li and Z. Chen, *Electrochim. Acta*, 2011, **56**, 5080.
20 E. L. Gyenge and J. F. Drillet, *J. Electrochem. Soc.*, 2012, **159**, F23.
21 E. Rasten, G. Hagen and R. Tunold, *Electrochim. Acta*, 2003, **48**, 3945.
22 I. Nikolov, R. Darkaoui, E. Zhecheva, R. Stoyanova, N. Dimitrov and T. Vitanov, *J. Electroanal. Chem.*, 1997, **429**, 157.
23 N. Fradette and B. Marsan, *J. Electrochem. Soc.*, 1998, **145**, 2320.
24 R. N. Singh, J. P. Pandey, N. K. Singh, B. Lal, P. Chartier and J. F. Koenig, *Electrochim. Acta*, 2000, **45**, 1911.
25 A. La Rosa-Toro, R. Berenguer, C. Quijada, F. Montilla, E. Morall and J. L. Vazquez, *J. Phys. Chem. B*, 2006, **110**, 24021.
26 F. Y. Cheng, J. Shen, B. Peng, Y. D. Pan, Z. L. Tao and J. Chen, *Nat. Mater.*, 2011, **3**, 79.
27 Z. Chen, A. Yu, D. Higgins, H. Li, H. Wang and Z. Chen, *Nano Lett.*, 2012, **12**, 1946.
28 M. Zhi, C. Xiang, J. Li, M. Li and N. Wu, *Nanoscale*, 2013, **5**, 72.
29 M. Zhi, N. Mariani, R. Gemmen, K. Gerdes and N. Wu, *Energy Environ. Sci.*, 2011, **4**, 417.
30 J. Luo, H. T. Zhu, H. M. Fan, J. K. Liang, H. L. Shi, G. H. Rao, J. B. Li, Z. M. Du and Z. X. Shen, *J. Phys. Chem. C*, 2008, **112**, 12594.
31 A. Fernández-Osorio, A. Vázquez-Olmos, R. Sato-Berru and R. Escudero, *Rev. Adv. Mater. Sci.*, 2009, **22**, 60.
32 A. L. M. Reddy, M. M. Shaijumon, S. R. Gowda and P. M. Ajayan, *Nano Lett.*, 2009, **9**, 1002.
33 M. Zhi, A. Manivannan, F. Meng and N. Wu, *J. Power Sources*, 2012, **208**, 345.
34 S. X. Mu, Z. P. Wu, Y. Wang, S. L. Qi, X. P. Yang and D. Z. Wu, *Thin Solid Films*, 2010, **518**, 4175.
35 B. J. Li, H. Q. Cao, J. Shao, G. Q. Li, M. Z. Qu and G. Yin, *Inorg. Chem.*, 2011, **50**, 1628.
36 J. J. Han, N. Li and T. Y. Zhang, *J. Power Sources*, 2009, **193**, 885.
37 T. H. Yang, S. Venkatesan, C. H. Lien, J. L. Chang and J. M. Zen, *Electrochim. Acta*, 2011, **56**, 6205.